Original Article

# Dynamic contrast-enhanced magnetic resonance imaging radiomics analysis based on intratumoral subregions for predicting luminal and nonluminal breast cancer

**Shuqian Feng[1], Jiandong Yin[2]**

[1]Department of Nuclear Medicine, Union Hospital, Tongji Medical College, Huazhong University of Science and Technology, Wuhan, China; [2]Department of Radiology, Shengjing Hospital of China Medical University, Shenyang, China

*Contributions:* (I) Conception and design: S Feng; (II) Administrative support: J Yin; (III) Provision of study materials or patients: J Yin; (IV) Collection and assembly of data: S Feng; (V) Data analysis and interpretation: S Feng; (VI) Manuscript writing: Both authors; (VII) Final approval of manuscript: Both authors.

*Correspondence to:* Jiandong Yin, PhD. Department of Radiology, Shengjing Hospital of China Medical University, No. 36, Sanhao Street, Heping District, Shenyang 110004, China. Email: jiandongyin@sina.com.

**Background:** Breast cancer is a heterogeneous disease with different morphological and biological characteristics. The molecular subtypes of breast cancer are closely related to the treatment and prognosis of patients. In order to predict the luminal type of breast cancer in a noninvasive manner, our study developed and validated a radiomics nomogram combining clinical factors with a radiomics score based on the features of the intratumoral subregion to distinguish between luminal and nonluminal breast cancer.

**Methods:** From January 2018 to January 2020, 153 women with clinically and pathologically diagnosed breast cancer with an average age of 50.08 years were retrospectively analyzed. Using a semiautomatic segmentation method, the whole tumor was divided into 3 subregions on the basis of the time required for the contrast agent to reach its peak; 540 features were extracted from 3 subregions and the whole tumor region. Subsequently, 2 machine learning classifiers were developed. The least absolute shrinkage and selection operator method was used for feature selection and radiomics score (Rad-score) construction. Moreover, multivariable logistic regression analysis was applied to select independent factors from the Rad-score and clinical factors to establish a prediction model in the form of a nomogram. The performance of the nomogram was evaluated through calibration, discrimination, and clinical usefulness.

**Results:** The prediction performance of texture features from the rapid subregion was the best in the 3 intratumoral subregions, and the area under the receiver operating characteristic curve (AUC) values in the training and validation cohort were 0.805 (95% CI: 0.719–0.892) and 0.737 (95% CI: 0.581–0.893), respectively. The Rad-score, consisting of 5 features from the rapid subregion, was associated with the luminal type of breast cancer (P=0.001 and P=0.035 in the training and validation cohorts, respectively). The predictors included in the personalized prediction nomogram included Rad-score, human epidermal growth factor receptor 2 (HER2) status, and tumor histological grade. The nomogram showed good discrimination, with an area under the receiver operating characteristic curve in the training and validation cohorts of 0.830 (95% CI: 0.746–0.896) and 0.879 (95% CI: 0.748–0.957), respectively. The calibration curve of the 2 cohorts and decision curve analysis demonstrated that the nomogram had good calibration and clinical usefulness.

**Conclusions:** We proposed a nomogram model that combined clinical factors and Rad-score, which showed good performance in predicting the luminal type of breast cancer.

**Keywords:** Dynamic contrast-enhanced magnetic resonance imaging (DCE-MRI); breast cancer; luminal; intratumoral subregion; radiomics

 

Submitted Oct 06, 2022. Accepted for publication Aug 14, 2023. Published online Sep 11, 2023.
doi: 10.21037/qims-22-1073
**View this article at:** https://dx.doi.org/10.21037/qims-22-1073

## Introduction

Breast cancer is the most common malignant tumor threatening women's health worldwide and one of the most common causes of cancer-related death in women. The incidence of breast cancer in most countries has been on the rise over the past few decades (1). Breast cancer is a heterogeneous disease with different morphological and biological characteristics (2,3). The molecular subtype of breast cancer is strongly linked to the treatment and prognosis of patients (4,5). Breast cancer can be divided into the luminal type and nonluminal type according to progesterone receptor (PR) and estrogen receptor (ER) expression (6). The luminal type, which includes luminal A and luminal B types, is sensitive to endocrine therapy and has a low rate of distant metastasis and good prognosis (7). The nonluminal type includes the human epidermal growth factor receptor 2 (HER2) overexpression type and triple-negative (TN) type, which are insensitive to endocrine therapy. Nonluminal breast cancer is more prone to tumor recurrence and metastasis and has a poor prognosis (8,9). The accurate determination of molecular subtypes is thus critical for the targeted treatment of patients with breast cancer.

Dynamic contrast-enhanced magnetic resonance imaging (DCE-MRI) can provide high-resolution tumor anatomical information and functional information related to angiogenesis and blood flow status (10-12). Data from DCE-MRI images have been used to quantitatively evaluate tumor heterogeneity and to establish prediction models for molecular subtypes or the ER/PR expression status of breast cancer (13-18). Lafcı *et al.* identified radiomics features that could distinguish luminal A from luminal B breast cancer by extracting and analyzing the features from T1-weighted DCE-MRI (16). In another study, Zhong *et al.* successfully constructed a radiomics score (Rad-score) to valuated ER and PR status in preoperative patients with breast cancer according to the texture features of the functional parameter maps calculated by breast DCE-MRI (17). These studies suggest that quantitative features from DCE-MRI images have the potential to predict lumen types in breast cancer.

Previous studies have obtained valuable information to quantify the extent of tumor heterogeneity based on the analysis of the whole tumor. However, intratumoral regions that exhibit different dynamic patterns may provide useful information that cannot be acquired by radiomics analysis of the whole tumor (19-21). The features extracted from intratumoral subregions have been used to predict the pathological complete response after neoadjuvant chemotherapy (NAC) (22,23). Other studies have examined the use of texture features inside tumors to distinguish between benign and malignant tumors, identify the HER2 status, and predict the amplification status of the Ki-67 index (24-26). However, it remains unclear whether intratumoral regional analysis is more effective than whole tumor analysis for differentiating the luminal types of breast cancer.

The purpose of this study was to establish a nomogram combining Rad-score and clinical factors for the personalized prediction of luminal and nonluminal breast cancer.

## Methods

### *Patients*

This study was conducted in accordance with the Declaration of Helsinki (revised in 2013) and approved by the Ethics Review Committee of Shengjing Hospital Affiliated to China Medical University. In view of the retrospective nature of this study, the need for informed consent was waived. Between January 2018 and January 2021, 300 patients with breast lesions detected with DCE-MRI were continuously collected and screened according to the following inclusion and exclusion criteria. The inclusion criteria were as follows: (I) breast DCE-MRI performed before biopsy or resection, and (II) available pathological results. The exclusion criteria were as follows: (I) incomplete pathological results, (II) patients who received chemotherapy or radiotherapy, and (III) presence of image artifacts. Finally, 153 female patients with a mean age of 50.08 years were included in the analysis and randomly divided into a training cohort (108 patients) and a validation cohort (45 patients). Clinical factors including age, HER2 status, Ki-67 status, histological grade, apparent diffusion coefficient (ADC) value, Breast Imaging Reporting & Data System (BI-RADS) category, and time–intensity curve (TIC) type were obtained from the imaging system. The flowchart of this study is shown in *Figure 1*.

 

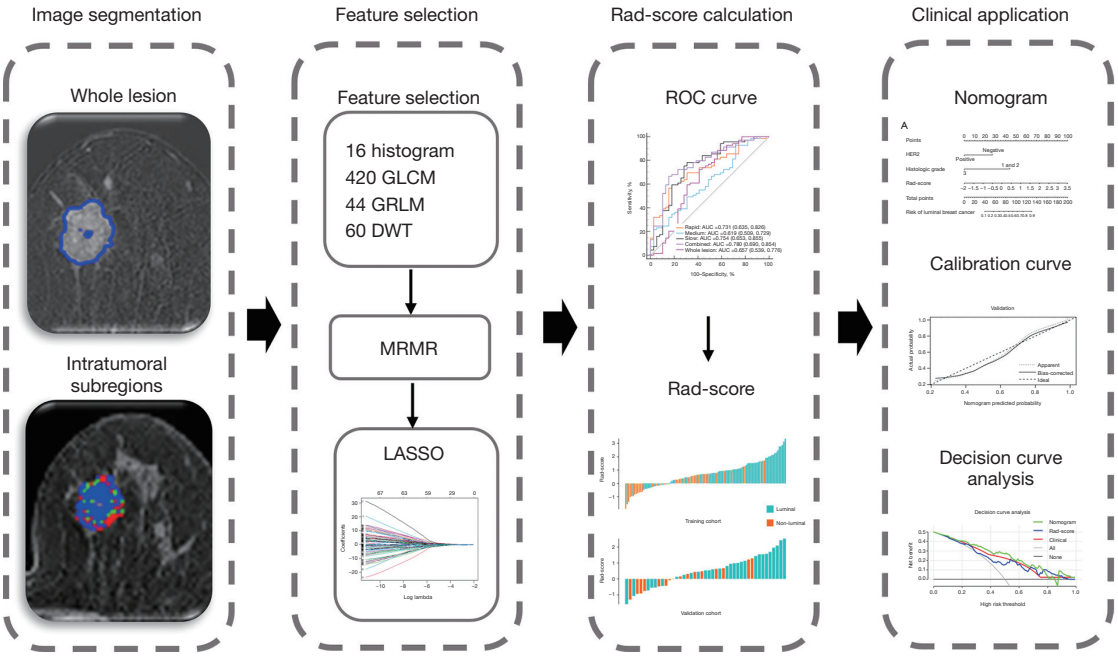


**Figure 1** Flowchart of the study. DWT, discrete wavelet transformation; GLCM, gray-level co-occurrence matrix; GLRLM, gray-level run-length matrix; LASSO, least absolute shrinkage and selection operator; MRMR, minimum redundancy maximum relevance; Rad-score, radiomics score; ROC, receiver operating characteristic.

### *Imaging protocol*

Detailed information on DCE-MRI image acquisition methods and imaging parameters are described in the Appendix 1.

### *Pathologic assessment*

ER, PR, and HER2 expression was detected using streptavidin peroxidase immunohistochemistry (IHC). The detailed pathological analysis is presented in Appendix 1.

### *Tumor segmentation*

A total of 3 experienced radiologists used the semiautomatic segmentation method to complete the segmentation of tumors and finally reached a consensus. The specific tumor segmentation methods are described in Appendix 1.

### *Intratumoral subregion partition*

To analyze tumor heterogeneity, the whole tumor area was divided into 3 subregions on the basis of the changes in pixel intensity at different imaging stages according to a previously reported method (26). Briefly, the specific approach proceeded follows:

First, the following equation was used to calculate the relative enhancement via comparing the postcontrast image and the pre-contrast image pixel by pixel:

$$E(p,q,t)=\frac{I(p,q,t)-I(p,q,t_0)}{I(p,q,t_0)} \quad [1]$$

where $I(p, q, t)$ and $I(p, q, t_0)$ represent the signal strength of the pixel $(p, q)$ obtained at times $t$ and $t_0$ (the precontrast moment) (27), and $E(p, q, t)$ is the time signal intensity curve, which depicts the variation of relative enhancement with time (28,29). Time to peak (TTP), the arrival time of peak enhancement, was calculated as follows:

$$TTP(p,q)=\arg\max_t E(p,q,t) \quad [2]$$

The pixels of the whole tumor region were then partitioned according to the TTP value. The lesion pixels that reached the peak enhancement value in the first to fourth, fifth or sixth, and seventh or eighth stages were divided into rapid, medium, and slow subregions, respectively. Therefore, the whole lesion was divided into 3 subregions representing different TTP values. *Figure 2* shows the tumor segmentation results of 2 random cases.

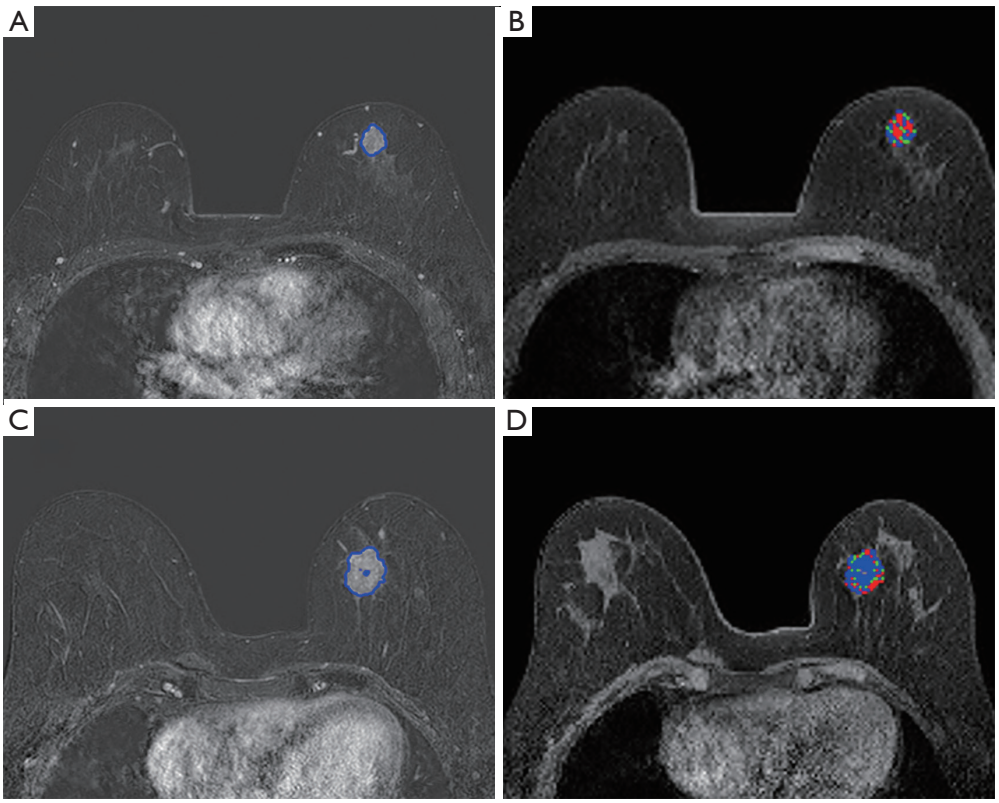


**Figure 2** Results of tumor segmentation. The first row shows an example of nonluminal breast cancer: (A) the result of segmenting the whole tumor region with semiautomatic method; (B) the result of intratumoral subregion division, with red, green, and blue representing rapid, medium, and slow subregions, respectively. The second row shows an example of luminal breast cancer: (C) the result of the whole tumor region; (D) the result of intratumoral subregions.

### *Feature extraction*

MATLAB 2018b (MathWorks) was used to extract 540 texture features from 3 intratumoral subregions and the whole tumor region, respectively. The extracted features were summarized into 4 types, information of which are provided in *Table 1*. For the detailed description of these features, please refer to Appendix 1. In the MRI subtraction image, the features extracted from the precontrast, median (the fourth), and last (the eighth) subtraction MR images were named S-0, S-4, and S-8 respectively. A precontrast sequence was included in the analysis based on previous studies showing that it was associated with the molecular type of breast cancer (15,30).

### *Interobserver variability assessment*

Readers 1 and 2 randomly selected 50 cases from all the out-of-order images for region of interest (ROI) segmentation and then extracted the features. The features were then evaluated using the intraclass correlation coefficient (ICC) (31). The features with ICC >0.8 were considered to have good reproducibility and stability and were retained for subsequent radiomics analysis.

### *Feature selection and radiomics score calculation*

From the features with good stability in the training cohort, 100 features with high correlation and low redundancy were selected using the minimum redundancy maximum relevance method. The least absolute shrinkage and selection operator method was then used to select the most useful prediction features from the dataset through 10-fold cross-validation, thereby reducing the dimension of the feature set (32). Support vector machine (SVM) and logistic regression (LR) classifiers were developed based on the features of each subregion, 3 subregions, and the whole

 

**Table 1** Details of extracted texture features

| Category | Texture features | Quantity |
|---|---|---|
| Histogram | Max, min, range, interquartile range, mean, median, standard, variance, skewness, kurtosis, covariance, 1st percentile, 10th percentile, 50th percentile, 90th percentile, 99th percentile | 16 |
| GLCM† | Autocorrelation (ACOR), contrast (CON), correlation (COR), cluster prominence (CP), cluster shade (CS), dissimilarity (DIS), joint energy (JENE), joint entropy (JENT), homogeneity (HOM), maximum probability (MP), sum of squares (SOS), sum average (SA), sum variance (SV), sum entropy (SE), difference variance (DV), difference entropy (DE), information measure of correlation 1 (IMC1), information measure of correlation 2 (IMC2), inverse difference normalized (IDN), inverse different moment (IDM), inverse difference moment normalized (IDMN) | 420 |
| GLRLM‡ | Run-length nonuniformity (RLN), gray-level nonuniformity (GLN), long-run emphasis (LRE), short-run emphasis (SRE), run percentage (RP), low gray-level run emphasis (LGLRE), high gray-level run emphasis (HGLRE), short-run low gray-level emphasis (SRLGLE), short-run high gray-level emphasis (SRHGLE), long-run low gray-level emphasis (LRLGLE), long-run high gray-level emphasis (LRHGLE) | 44 |
| DWT§ | Harr parameters | 20 |
| | Daubechies2 parameters | 20 |
| | Symlet4 parameters | 20 |
| Total | | 540 |

†, GLCM parameters were calculated for 4 distances (1, 2, 3, and 4 pixels) and 4 angles (0°, 45°, 90°, and 135°). (d, 0), (0, d), (d, d), and (–d, –d) represent 0°, 45°, 90°, and 135°, respectively, where d is the distance. For example, CON (0, 1) represents the contrast feature calculated for a distance of 1 and a direction of 90°. ‡, GLRLM parameters were calculated for 4 angles (0°, 45°, 90°, and 135°). §, DWT parameters were calculated for 4 layers and 3 directions (horizontal, vertical, diagonal) to produce low and high frequency components. For example, Harr_4_H_V represents the vertical high frequency component of the fourth layer using the Harr wavelet. DWT, discrete wavelet transformation; GLCM, gray-level co-occurrence matrix; GLRLM, gray-level run-length matrix.

region, and their discrimination performance was evaluated using the area under the receiver operating characteristic (ROC) curve (AUC). Finally, the Rad-score of each patient was calculated according to the linear combination of the respective coefficient weights of the selected features.

### *Development of the nomogram*

A nomogram for predicting luminal and nonluminal breast cancer was developed using data from the training cohort. Univariate and multivariate logistic regression analyses were performed to identify important factors associated with the luminal classification of breast cancer. Candidate factors included all clinical factors. Factors with P<0.1 in univariate analyses were included in multivariate analyses (33). The Akaike information criterion was used as the likelihood ratio test of the stop rule, and forward step-by-step selection was applied for multivariate analysis in the training cohort. The variance inflation factor (VIF) was used to estimate the collinearity diagnosis of multivariable logistic regression. Finally, the independently predicted values were combined to obtain a nomogram.

### *Validation of the nomogram*

ROC curves were drawn to assess the performance of the nomogram for differentiating luminal and nonluminal breast cancer in the training and validation cohorts, and the AUC was calculated to quantify discrimination. The calibration curve was drawn to analyze the consistency between the predicted risk and observed risk of luminal breast cancer for determining the prediction accuracy of the nomogram in 2 cohorts (34). By quantifying the net benefit of different threshold probabilities in the validation cohort, decision curve analysis (DCA) was performed to determine the clinical usefulness of the nomogram (35).

### *Statistical analysis*

SPSS 23.0 and R software (version 4.4.1) were used for statistical analyses, while the $\chi^2$ test was used for comparative analyses. Continuous variables satisfying the normal distribution were compared with Student *t* test. The Mann-Whitney test was used to compare continuous variables with nonnormal or unknown distribution. Two-

 

**Table 2** Characteristics of the patients in the training and validation cohorts

| Characteristics | Training cohort (n=108) | | | Validation cohort (n=45) | | | P† |
|---|---|---|---|---|---|---|---|
| | Nonluminal (n=39) | Luminal (n=69) | P | Nonluminal (n=16) | Luminal (n=29) | P | |
| Age, mean ± SD, years | 51.90±9.86 | 48.17±8.95 | 0.048 | 50.00±7.49 | 52.21±10.50 | 0.463 | 0.278 |
| ADC value, median (IQR) | 1.06 (0.96, 1.23) | 0.98 (0.85, 1.08) | 0.015 | 1.06 (0.90, 1.15) | 0.90 (0.83, 1.08) | 0.046 | 0.322 |
| TIC, % | | | 0.664 | | | 0.900 | 0.137 |
| Wash-out | 29 (74.36) | 48 (69.57) | | 13 (81.25) | 24 (82.75) | | |
| Plateau | 8 (20.51) | 19 (27.53) | | 3 (18.75) | 5 (17.25) | | |
| Wash-in | 2 (5.13) | 2 (2.89) | | 0 (0.00) | 0 (0.00) | | |
| BI-RADS, % | | | 0.168 | | | 0.104 | 0.822 |
| 4A | 0 (0.00) | 2 (2.90) | | 0 (0.00) | 0 (0.00) | | |
| 4B | 5 (12.82) | 10 (14.49) | | 2 (12.50) | 6 (20.69) | | |
| 4C | 22 (56.41) | 44 (63.77) | | 8 (50.00) | 19 (65.52) | | |
| 5 | 12 (30.77) | 13 (18.84) | | 6 (37.50) | 4 (13.79) | | |
| Ki-67, % | | | 0.730 | | | 0.742 | 0.716 |
| Low | 9 (23.08) | 18 (26.09) | | 4 (25.00) | 6 (20.69) | | |
| High | 30 (76.12) | 51 (73.91) | | 12 (75.00) | 23 (79.31) | | |
| HER2, % | | | <0.001 | | | 0.003 | 0.019 |
| Negative | 13 (33.33) | 48 (69.57) | | 1 (6.25) | 15 (51.72) | | |
| Positive | 26 (66.67) | 21 (30.43) | | 15 (93.75) | 14 (48.28) | | |
| Histologic grade, % | | | 0.001 | | | 0.017 | 0.531 |
| I and II | 26 (66.67) | 65 (94.20) | | 10 (62.50) | 27 (93.10) | | |
| III | 13 (33.33) | 4 (5.80) | | 6 (37.50) | 2 (6.90) | | |
| Rad-score, median (IQR) | 0.25 (–0.19, 0.58) | 0.98 (0.37, 1.56) | <0.001 | 0.10 (–0.55, 0.53) | 0.81 (0.25, 1.54) | 0.017 | 0.200 |

P value was obtained from univariate association analysis between each clinicopathological variable and breast cancer type. P† indicates the comparative analysis between the training cohort and the validation cohort. ADC, apparent diffusion coefficient; BI-RADS, breast imaging reporting and data system; HER2, human epidermal growth factor receptor 2; IQR, interquartile range; Rad-score, radiomics score; SD, standard deviation; TIC, time-intensity curve.

sided P values <0.05 were considered statistically significant. The ROC curve was drawn with the maximum Youden Index as the best cutoff value, and AUC, sensitivity, specificity, accuracy, positive predictive value, and negative predictive value were calculated as comparison indicators (36,37). Delong test was used to statistically compare the AUC values of the 2 models (38). ROC curves were plotted using MedCalc software (version 20.0, MedCalc Software Ltd.).

## Results

### *Clinical characteristics*

*Table 2* shows the basic information of the study cohort. HER2 status differed significantly between the 2 cohorts (P=0.019), but there was no significant difference between the 2 cohorts in other basic clinical characteristics (P>0.05). Other details of patients are shown in *Table 2*.

### *Feature selection and radiomics score calculation*

Finally, 1,598, 1,603, 1,582, and 1,611 features in the rapid subregion, medium subregion, slow subregion, and whole tumor region showed good stability, respectively, with 5, 1, 5, and 1 effective features being left after the feature selection step, respectively. *Table 3* lists each feature in detail and shows their predictive performance. In general,

 

**Table 3** Predictive performance of selected features from 3 subregions and the entire tumor region

| Method | Subregions | Feature | Cohort | AUC | Interval | P† |
|---|---|---|---|---|---|---|
| Intratumoral Regionalization | Rapid | Skewness (S-0) | Training | 0.796 | 0.705–0.888 | 0.032 |
| | | | Validation | 0.726 | 0.570–0.882 | 0.078 |
| | | Daubechies2_4_H_V (S-0) | Training | 0.548 | 0.535–0.603 | 0.021 |
| | | | Validation | 0.515 | 0.315–0.715 | 0.813 |
| | | SRHGLE_0 (S-4) | Training | 0.741 | 0.646–0.836 | 0.128 |
| | | | Validation | 0.584 | 0.397–0.771 | 0.599 |
| | | GLN_135 (S-4) | Training | 0.628 | 0.514–0.743 | 0.969 |
| | | | Validation | 0.621 | 0.434–0.807 | 0.417 |
| | | Skewness (S-8) | Training | 0.805 | 0.719–0.892 | 0.011 |
| | | | Validation | 0.737 | 0.581–0.893 | 0.085 |
| | Medium | Daubechies2_4_H_V (S-4) | Training | 0.724 | 0.624–0.825 | 0.263 |
| | | | Validation | 0.640 | 0.468–0.812 | 0.347 |
| | Slow | Skewness (S-0) | Training | 0.651 | 0.538–0.764 | 0.816 |
| | | | Validation | 0.608 | 0.417–0.799 | 0.546 |
| | | Skewness (S-4) | Training | 0.713 | 0.613–0.813 | 0.299 |
| | | | Validation | 0.616 | 0.436–0.797 | 0.458 |
| | | RP_0 (S-4) | Training | 0.604 | 0.493–0.716 | 0.745 |
| | | | Validation | 0.625 | 0.450–0.800 | 0.414 |
| | | Harr_4_H_H (S-4) | Training | 0.639 | 0.528–0.751 | 0.930 |
| | | | Validation | 0.621 | 0.437–0.805 | 0.444 |
| | | Harr_4_H_D (S-4) | Training | 0.742 | 0.638–0.846 | 0.142 |
| | | | Validation | 0.603 | 0.436–0.771 | 0.451 |
| Whole Lesion | – | Covariance (S-8) | Training | 0.632 | 0.520–0.744 | – |
| | | | Validation | 0.522 | 0.343–0.701 | – |

†, P value represents the performance comparison between the features from the intratumoral subregions and the feature from the whole tumor region. AUC, area under the receiver operating characteristic curve; SRHGLE, short-run high gray-level emphasis; GLN, gray-level nonuniformity; RP, run percentage.

the features belonging to the rapid subregion performed best in the 3 subregions, and the highest AUC values in the training and validation cohort were 0.805 and 0.737, respectively. In the training cohort, the AUC values for skewness (S-0), Daubechies wavelet 24 HV (S-0), and skewness (S-8) from the rapid subregion were higher than those of the whole tumor region, with P values of 0.032, 0.021, and 0.011, respectively.

*Tables 4*,*5* show the performance of the 2 classifier models in identifying the luminal and nonluminal breast cancer in 2 cohorts. The relevant ROC curves are shown in *Figure 3A-3D*. Regardless of the classifier, the features belonging to the rapid subregion showed the most stable classification performance. The Delong test results of each classification model are shown in Table S1.

According to the analysis results, we selected the features extracted from the rapid subregion to calculate the Rad-score. The corresponding calculation formula is provided in the Appendix 1. There was no significant difference in the distribution of Rad-scores between the training and

 

**Table 4** The performance of the SVM classifier in distinguishing between luminal and nonluminal breast cancer.

| Regions | Cohort | AUC (95% CI) | SEN (%) | SPE (%) | ACC (%) | PPV (%) | NPV (%) |
|---|---|---|---|---|---|---|---|
| Rapid | Training | 0.731 (0.635, 0.826) | 59.42 | 82.05 | 69.44 | 69.14 | 71.43 |
| | Validation | 0.736 (0.626, 0.900) | 51.72 | 100 | 66.67 | 70.59 | 54.55 |
| Medium | Training | 0.619 (0.509, 0.729) | 92.75 | 28.21 | 67.59 | 67.00 | 75.00 |
| | Validation | 0.681 (0.519, 0.843) | 51.72 | 81.25 | 55.56 | 60.98 | 0.00 |
| Slow | Training | 0.754 (0.653, 0.855) | 78.26 | 69.23 | 71.30 | 70.21 | 78.57 |
| | Validation | 0.656 (0.494, 0.817) | 41.38 | 93.75 | 64.44 | 71.88 | 46.15 |
| Combined | Training | 0.780 (0.690, 0.854) | 63.77 | 76.82 | 72.97 | 75.78 | 78.60 |
| | Validation | 0.692 (0.537, 0.821) | 52.46 | 56.25 | 61.20 | 65.23 | 50.20 |
| Whole lesion | Training | 0.657 (0.539, 0.776) | 88.41 | 43.59 | 71.30 | 69.39 | 90.00 |
| | Validation | 0.616 (0.448, 0.785) | 55.17 | 75.00 | 55.56 | 60.97 | 0.00 |

ACC, accuracy; AUC, area under the receiver operating characteristic curve; CI, confidence interval; NPV, negative predictive value; PPV, positive predictive value; SEN, sensitivity; SPE, specificity; SVM, support vector machine.

**Table 5** The performance of the LR classifier in distinguishing between luminal and nonluminal breast cancer

| Regions | Cohort | AUC (95% CI) | SEN (%) | SPE (%) | ACC (%) | PPV (%) | NPV (%) |
|---|---|---|---|---|---|---|---|
| Rapid | Training | 0.744 (0.651, 0.823) | 63.77 | 82.05 | 70.37 | 86.27 | 56.14 |
| | Validation | 0.718 (0.564, 0.842) | 65.52 | 75.00 | 68.89 | 82.61 | 54.55 |
| Medium | Training | 0.623 (0.525, 0.715) | 62.32 | 58.97 | 61.11 | 72.88 | 46.94 |
| | Validation | 0.578 (0.421, 0.723) | 48.28 | 81.25 | 60.00 | 82.35 | 46.43 |
| Slow | Training | 0.755 (0.663, 0.832) | 66.67 | 76.92 | 70.37 | 86.27 | 56.14 |
| | Validation | 0.616 (0.460, 0.757) | 48.28 | 81.25 | 60.00 | 82.35 | 46.43 |
| Combined | Training | 0.804 (0.716, 0.874) | 73.54 | 66.25 | 74.87 | 90.06 | 69.65 |
| | Validation | 0.634 (0.477, 0.772) | 59.45 | 72.50 | 62.69 | 84.37 | 41.84 |
| Whole lesion | Training | 0.597 (0.498, 0.690) | 17.39 | 100.00 | 47.22 | 100 | 40.63 |
| | Validation | 0.571 (0.415, 0.718) | 72.41 | 56.25 | 66.67 | 75.00 | 52.94 |

ACC, accuracy; AUC, area under the receiver operating characteristic curve; CI, confidence interval; LR, logistic regression; NPV, negative predictive value; PPV, positive predictive value; SEN, sensitivity; SPE, specificity.

validation cohort (P=0.200). Patients with luminal breast cancer had higher Rad-scores (*Table 2*). The bar graph in Figure S1 shows the good discrimination performance of the Rad-score.

### *Development of the nomogram*

Rad-score, HER2 status, and histological grade were identified as independent predictors according to the results of logistic regression analysis. The VIF was 1.050–1.117, indicating that all variables were not collinear. The independent predictors identified were used to develop a prediction model in the form of a nomogram (*Figure 4A*).

### *Validation of the nomogram*

*Table 6* shows the performance of the nomogram, clinical factors, and Rad-score for distinguishing the luminal types of breast cancer. The AUC values for the nomogram, clinical factors, and Rad-score were 0.830 (95% CI: 0.746–

 

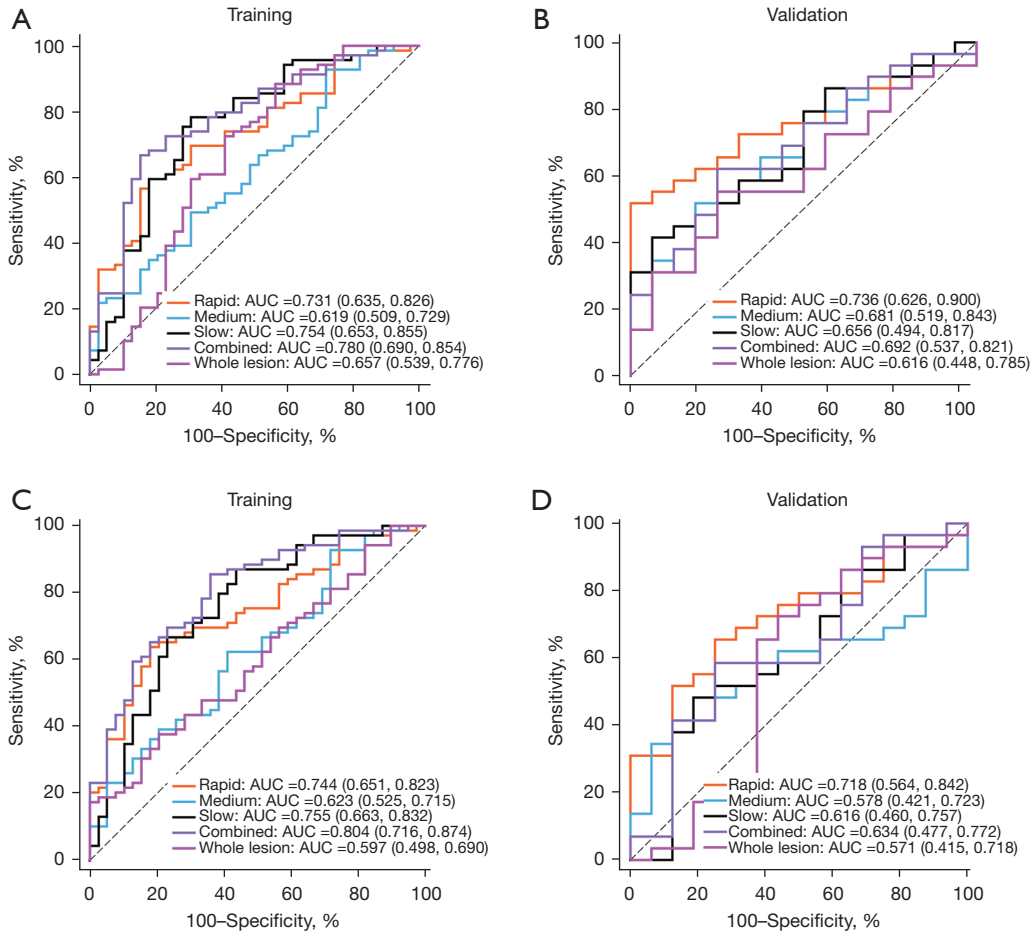


**Figure 3** ROC curves of the performance of 2 machine learning classifiers in the training cohort and the validation cohort. ROC curves of the SVM classifier in the training (A) and verification cohort (B). ROC curves of the LR classifier in the training (C) and validation cohorts (D). ROC, receiver operating characteristic; AUC, area under the ROC curve; SVM, support vector machine; LR, logistic regression.

0.896), 0.766 (95% CI: 0.675–0.842), and 0.744 (95% CI: 0.651–0.823) in the training cohort and 0.879 (95% CI: 0.748–0.957), 0.781 (95% CI: 0.633–0.891), and 0.718 (95% CI: 0.564–0.842) in the validation cohort, respectively. In the training cohort, the performance of the nomogram was better than that of any single clinical variable (P=0.016) and Rad-score (P=0.023). The performance of the nomogram in the validation cohort was also better than that of the Rad-score (P=0.017). Clinical predictors and Rad-score showed similar discrimination performance in the 2 cohorts. The calibration curves (*Figure 4B*,*4C*) showed good consistency between predictions and observations. *Figure 4D*,*4E* showed the ROC curves of the nomogram, clinical factors, and Rad-score performance in differentiating luminal types in each cohort.

As shown in *Figure 5*, the DCA results supported the clinical usefulness of the nomogram. The greatest benefits of the nomogram model were obtained when the threshold probability was in the range of 3–82%. The use of the nomogram to identify luminal breast cancer was more effective than was using only clinical variables or Rad-score.

## Discussion

In this study, we used the intratumoral partitioning method to divide the tumor region into 3 subregions and extract features to differentiate between luminal and nonluminal breast cancer. The ROC curves indicated that the features belonging to the rapid subregion had the best performance. The Rad-score was calculated with these features, and a nomogram model was established including Rad-score, HER2 status, and histological grade. The results

 

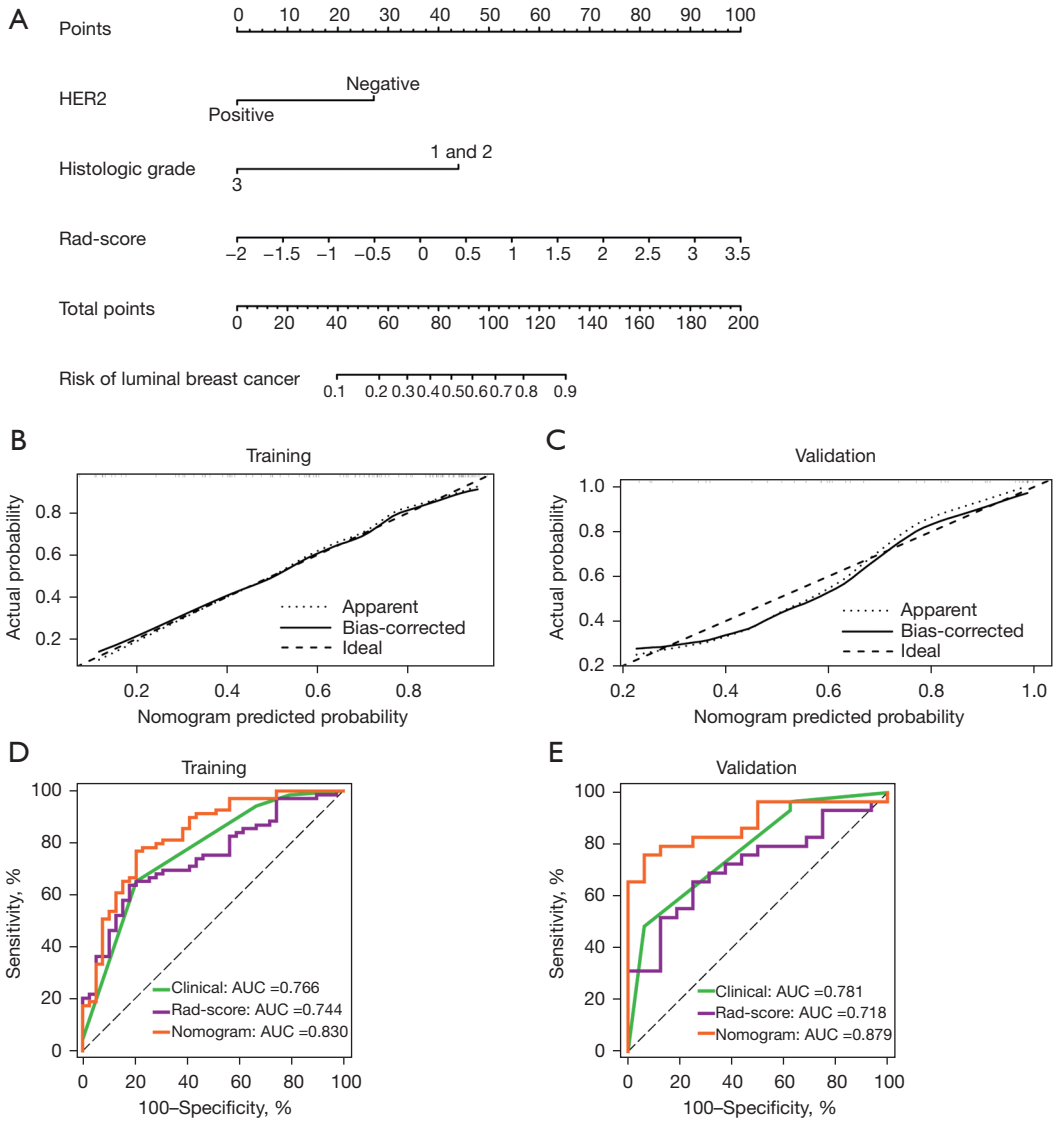


**Figure 4** Establishment and evaluation of the nomogram model. (A) The developed nomogram containing Rad-score, HER2 status, and histological grade. (B and C) Calibration curves of the nomogram for the training (B) and validation cohorts (C). (D and E) ROC curves of the nomogram, clinical predictors, and Rad-score for the training (D) and validation cohorts (E). HER2, human epidermal growth factor receptor 2; Rad-score, radiomics score; AUC, area under the ROC curve; ROC, receiver operating characteristic.

demonstrated that the nomogram had good discrimination and calibration performance, and DCA supported its clinical usefulness.

In the analysis of tumor heterogeneity, most previous studies included the whole tumor region through various sequences based on DCE-MRI (13,15,39,40). However, tumor subregions with different dynamic enhancement patterns are associated with different biological processes and thus different prognoses, and they may have valuable information that cannot be captured by analyzing the whole tumor (19,27,41,42). Wu *et al.* collected 4 quantitative Haralick texture features in each tumor subregion based on gray-level co-occurrence matrix (GLCM) and used the changes of texture features to predict the pathological complete response after neoadjuvant chemotherapy. The AUC of the features from the intratumor subregion was between 0.75 and 0.80, which was significantly better than the texture analysis based on the whole lesion (AUC =0.65) (22).

 

**Table 6** The predictive performance of the nomogram, clinical predictors, and Rad-score

| Cohort | Nomogram | Clinical | Rad-score | P | | |
|---|---|---|---|---|---|---|
| | | | | Nomogram *vs.* clinical | Nomogram *vs.* Rad-score | Clinical *vs.* Rad-score |
| Training cohort (n=108) | | | | 0.016 | 0.023 | 0.708 |
| AUC (95% CI) | 0.830 (0.746, 0. 896) | 0.766 (0.675, 0.842) | 0.744 (0.651, 0.823) | | | |
| ACC | 0.778 | 0.704 | 0.704 | | | |
| SEN | 0.768 | 0.652 | 0.638 | | | |
| SPE | 0.795 | 0.795 | 0.821 | | | |
| Validation cohort (n=45) | | | | 0.068 | 0.017 | 0.546 |
| AUC (95% CI) | 0.879 (0.748, 0.957) | 0.781 (0.633, 0.891) | 0.718 (0.564, 0.842) | | | |
| ACC | 0.822 | 0.644 | 0.689 | | | |
| SEN | 0.759 | 0.483 | 0.655 | | | |
| SPE | 0.938 | 0.75 | 0.938 | | | |

ACC, accuracy; AUC, area under the receiver operating characteristic curve; CI, confidence interval; Rad-score, radiomics score; SEN, sensitivity; SPE, specificity.

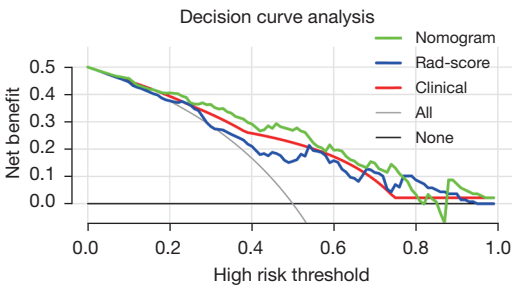


**Figure 5** Decision curve analysis of the nomogram, clinical factors, and Rad-score. The green line represents the nomogram, the blue line represents the Rad-score, the red line represents the clinical factors, the gray line represents the hypothesis that all patients have luminal breast cancer, and the black line represents the hypothesis that all patients have nonluminal breast cancer. Rad-score, radiomics score.

In this study, we extracted features from the whole tumor lesion and 3 intratumoral subregions segmented based on TTP values and then established classifier models to distinguish between luminal and nonluminal breast cancer. Finally, the predictive performance of the LR model constructed with features from the rapid and slow subregions in the training cohort was found to be better than the model based on the whole tumor region (P=0.023, P=0.047). One possible explanation for this result is that these tumor subregions may embody angiogenesis, which may reflect the biomarker status related to different types of tumors (13,43).

Intratumoral heterogeneity refers to differences in biological characteristics, such as gene expression, angiogenesis, and metabolism (20,44). The close correlation between the microscopic characteristics of medical images and the microstructure and biological characteristics of tumors has been confirmed (45,46). However, the correlation between tumor biological characteristics and radiomics features is complex, and identifying suitable biomarkers to understand the relationship between radiomics features and biological behavior is challenging (47). One useful approach is to use radiomics to identify multiple parameters for the construction of prediction models (48,49). In this study, a Rad-score was developed using 5 features from the rapid subregion. The features used to calculate Rad-score were mainly histogram and gray-level run length matrix (GLRLM). Histogram features can describe the distribution of voxel intensity in the image area, and GLRLM can quantify the gray-level run of continuous pixels with the same gray value. Rad-score, which combines these features, performed well as an independent predictor in distinguishing luminal types, with AUC values in the training and validation cohorts of 0.744 and 0.718, respectively.

Routine clinical testing of molecular subtypes of breast

 

cancer relies on invasive tissue sampling and genetic analysis, which is inherently limited because biopsies performed at a single point in time do not reflect genetic heterogeneity within the breast tumor (50,51). At present, the prediction of breast molecular subtypes requires not only a doctor's visual examination but simultaneous IHC as well. IHC is a method of tissue sampling that both time-consuming invasive to patients. In addition, in order to more accurately determine the molecular typing of the breast, further fluorescence *in situ* hybridization analysis is needed, further increasing the time and cost of the procedure. In our study, quantitative features were extracted and analyzed from medical images, and the extracted features were used for screening modeling to predict breast cancer luminal types noninvasively. Meanwhile, a nomogram combining clinicopathological factors and Rad-score was also proposed. The use of nomograms for predicting prognosis and results is common. Previous studies have shown that a nomogram model, that combined Rad-score and clinical factors had better predictive performance than radiomics model or clinical model alone (52-55). In Luo *et al.*'s study (52), Rad-score, HER2 status, and tumor histological grade were independent predictors of luminal breast cancer. HER2-positive status was significantly associated with nonluminal breast cancer, which was consistent with previous research (56). The nomogram combined these 3 variables to differentiate luminal and nonluminal breast cancer and showed good discrimination performance (AUC =0.879), which was significantly better than that of the Rad-score in the validation cohort (P=0.017). This suggests that the combination of the Rad-score and clinical factors can improve the diagnostic performance of the radiomics model. Several recent studies support the value of combining the Rad-score and clinical factors in establishing radiomics models to predict tumor molecular type (56-58). The results of DCA confirmed the usefulness of the nomogram for clinical application and demonstrated that the nomogram was more effective for predicting breast tumor types than was the all-treatment scheme (assuming that all breast tumors were luminal) or no-treatment scheme (assuming that all breast tumors were nonluminal).

This study had several limitations. First, the sample size was small, and patient data were obtained from a single hospital. Second, we analyzed single-layer images obtained at the largest cross-section of the representative tumor, which might have led to the omission of useful information regarding the tumor (59). Third, the inclusion of a greater number of radiomics features and the combination of DCE-MRI with other imaging methods could improve the accuracy of prediction. Finally, the complexity of the process for calculating the Rad-score in this study may present obstacles to its implementation in daily practice. In future research, efforts will be made to find more simplified biomarkers.

## Conclusions

In conclusion, this study proposed a nomogram combining clinical factors and Rad-score, which performed well in distinguishing luminal and nonluminal breast cancer. Further validation of the present results is needed before the clinical application of the model.

## Acknowledgments

We would like to thank International Science Editing (http://www.internationalscienceediting.com) for editing this manuscript.
*Funding:* None.

## Footnote

*Conflicts of Interest:* Both authors have completed the ICMJE uniform disclosure form (available at https://qims.amegroups.com/article/view/10.21037/qims-22-1073/coif). The authors have no conflicts of interest to declare.

*Ethical Statement:* The authors are accountable for all aspects of the work in ensuring that questions related to the accuracy or integrity of any part of the work are appropriately investigated and resolved. The study was conducted in accordance with the Declaration of Helsinki (as revised in 2013) and was approved by the Ethics Review Committee of Shengjing Hospital Affiliated to China Medical University. In view of the retrospective nature of this study, individual consent for this retrospective analysis was waived.



 

## References


1. Siegel RL, Miller KD, Jemal A. Cancer statistics, 2020. CA Cancer J Clin 2020;70:7-30.
2. Weigelt B, Geyer FC, Reis-Filho JS. Histological types of breast cancer: how special are they? Mol Oncol 2010;4:192-208.
3. Abramson VG, Lehmann BD, Ballinger TJ, Pietenpol JA. Subtyping of triple-negative breast cancer: implications for therapy. Cancer 2015;121:8-16.
4. Sanges F, Floris M, Cossu-Rocca P, Muroni MR, Pira G, Urru SAM, et al. Histologic subtyping affecting outcome of triple negative breast cancer: a large Sardinian population-based analysis. BMC Cancer 2020;20:491.
5. Dawood S, Hu R, Homes MD, Collins LC, Schnitt SJ, Connolly J, Colditz GA, Tamimi RM. Defining breast cancer prognosis based on molecular phenotypes: results from a large cohort study. Breast Cancer Res Treat 2011;126:185-92.
6. Dai X, Xiang L, Li T, Bai Z. Cancer Hallmarks, Biomarkers and Breast Cancer Molecular Subtypes. J Cancer 2016;7:1281-94.
7. Schnitt SJ. Classification and prognosis of invasive breast cancer: from morphology to molecular taxonomy. Mod Pathol 2010;23 Suppl 2:S60-4.
8. Su Y, Zheng Y, Zheng W, Gu K, Chen Z, Li G, Cai Q, Lu W, Shu XO. Distinct distribution and prognostic significance of molecular subtypes of breast cancer in Chinese women: a population-based cohort study. BMC Cancer 2011;11:292.
9. Engstrøm MJ, Opdahl S, Hagen AI, Romundstad PR, Akslen LA, Haugen OA, Vatten LJ, Bofin AM. Molecular subtypes, histopathological grade and survival in a historic cohort of breast cancer patients. Breast Cancer Res Treat 2013;140:463-73.
10. Nagy JA, Chang SH, Dvorak AM, Dvorak HF. Why are tumour blood vessels abnormal and why is it important to know? Br J Cancer 2009;100:865-9.
11. Karahaliou A, Vassiou K, Arikidis NS, Skiadopoulos S, Kanavou T, Costaridou L. Assessing heterogeneity of lesion enhancement kinetics in dynamic contrast-enhanced MRI for breast cancer diagnosis. Br J Radiol 2010;83:296-309.
12. Pinker K, Helbich TH, Morris EA. The potential of multiparametric MRI of the breast. Br J Radiol 2017;90:20160715.
13. Mazurowski MA, Zhang J, Grimm LJ, Yoon SC, Silber JI. Radiogenomic analysis of breast cancer: luminal B molecular subtype is associated with enhancement dynamics at MR imaging. Radiology 2014;273:365-72.
14. Yamaguchi K, Abe H, Newstead GM, Egashira R, Nakazono T, Imaizumi T, Irie H. Intratumoral heterogeneity of the distribution of kinetic parameters in breast cancer: comparison based on the molecular subtypes of invasive breast cancer. Breast Cancer 2015;22:496-502.
15. Sutton EJ, Dashevsky BZ, Oh JH, Veeraraghavan H, Apte AP, Thakur SB, Morris EA, Deasy JO. Breast cancer molecular subtype classifier that incorporates MRI features. J Magn Reson Imaging 2016;44:122-9.
16. Lafcı O, Celepli P, Seher Öztekin P, Koşar PN. DCE-MRI Radiomics Analysis in Differentiating Luminal A and Luminal B Breast Cancer Molecular Subtypes. Acad Radiol 2023;30:22-9.
17. Zhong S, Wang F, Wang Z, Zhou M, Li C, Yin J. Multiregional Radiomic Signatures Based on Functional Parametric Maps from DCE-MRI for Preoperative Identification of Estrogen Receptor and Progesterone Receptor Status in Breast Cancer. Diagnostics (Basel) 2022.
18. Monti S, Aiello M, Incoronato M, Grimaldi AM, Moscarino M, Mirabelli P, Ferbo U, Cavaliere C, Salvatore M. DCE-MRI Pharmacokinetic-Based Phenotyping of Invasive Ductal Carcinoma: A Radiomic Study for Prediction of Histological Outcomes. Contrast Media Mol Imaging 2018;2018:5076269.
19. Chaudhury B, Zhou M, Goldgof DB, Hall LO, Gatenby RA, Gillies RJ, Patel BK, Weinfurtner RJ, Drukteinis JS. Heterogeneity in intratumoral regions with rapid gadolinium washout correlates with estrogen receptor status and nodal metastasis. J Magn Reson Imaging 2015;42:1421-30.
20. Marusyk A, Polyak K. Tumor heterogeneity: causes and consequences. Biochim Biophys Acta 2010;1805:105-17.
21. Carvalho ED, Filho AOC, Silva RRV, Araújo FHD, Diniz JOB, Silva AC, Paiva AC, Gattass M. Breast cancer diagnosis from histopathological images using textural features and CBIR. Artif Intell Med 2020;105:101845.
22. Wu J, Gong G, Cui Y, Li R. Intratumor partitioning and texture analysis of dynamic contrast-enhanced (DCE)-MRI identifies relevant tumor subregions to predict pathological response of breast cancer to neoadjuvant chemotherapy. J Magn Reson Imaging 2016;44:1107-15.
23. Braman NM, Etesami M, Prasanna P, Dubchuk C, Gilmore H, Tiwari P, Plecha D, Madabhushi A. Intratumoral and peritumoral radiomics for the


 

pretreatment prediction of pathological complete response to neoadjuvant chemotherapy based on breast DCE-MRI. Breast Cancer Res 2017;19:57.
24. Zhang B, Song L, Yin J. Texture Analysis of DCE-MRI Intratumoral Subregions to Identify Benign and Malignant Breast Tumors. Front Oncol 2021;11:688182.
25. Lu H, Yin J. Texture Analysis of Breast DCE-MRI Based on Intratumoral Subregions for Predicting HER2 2+ Status. Front Oncol 2020;10:543.
26. Fan M, Cheng H, Zhang P, Gao X, Zhang J, Shao G, Li L. DCE-MRI texture analysis with tumor subregion partitioning for predicting Ki-67 status of estrogen receptor-positive breast cancers. J Magn Reson Imaging 2018;48:237-47.
27. Ashraf A, Gaonkar B, Mies C, DeMichele A, Rosen M, Davatzikos C, Kontos D. Breast DCE-MRI Kinetic Heterogeneity Tumor Markers: Preliminary Associations With Neoadjuvant Chemotherapy Response. Transl Oncol 2015;8:154-62.
28. Gu J, Polley EC, Denis M, Carter JM, Pruthi S, Gregory AV, Boughey JC, Fazzio RT, Fatemi M, Alizad A. Early assessment of shear wave elastography parameters foresees the response to neoadjuvant chemotherapy in patients with invasive breast cancer. Breast Cancer Res 2021;23:52.
29. Lee SH, Kim JH, Cho N, Park JS, Yang Z, Jung YS, Moon WK. Multilevel analysis of spatiotemporal association features for differentiation of tumor enhancement patterns in breast DCE-MRI. Med Phys 2010;37:3940-56.
30. Fan M, Li H, Wang S, Zheng B, Zhang J, Li L. Radiomic analysis reveals DCE-MRI features for prediction of molecular subtypes of breast cancer. PLoS One 2017;12:e0171683.
31. Xue C, Yuan J, Lo GG, Chang ATY, Poon DMC, Wong OL, Zhou Y, Chu WCW. Radiomics feature reliability assessed by intraclass correlation coefficient: a systematic review. Quant Imaging Med Surg 2021;11:4431-60.
32. Sauerbrei W, Royston P, Binder H. Selection of important variables and determination of functional form for continuous predictors in multivariable model building. Stat Med 2007;26:5512-28.
33. Cai J, Zheng J, Shen J, Yuan Z, Xie M, Gao M, Tan H, Liang Z, Rong X, Li Y, Li H, Jiang J, Zhao H, Argyriou AA, Chua MLK, Tang Y. A Radiomics Model for Predicting the Response to Bevacizumab in Brain Necrosis after Radiotherapy. Clin Cancer Res 2020;26:5438-47.
34. Coutant C, Olivier C, Lambaudie E, Fondrinier E, Marchal F, Guillemin F, Seince N, Thomas V, Levêque J, Barranger E, Darai E, Uzan S, Houvenaeghel G, Rouzier R. Comparison of models to predict nonsentinel lymph node status in breast cancer patients with metastatic sentinel lymph nodes: a prospective multicenter study. J Clin Oncol 2009;27:2800-8.
35. Vickers AJ, Cronin AM, Elkin EB, Gonen M. Extensions to decision curve analysis, a novel method for evaluating diagnostic tests, prediction models and molecular markers. BMC Med Inform Decis Mak 2008;8:53.
36. Ruopp MD, Perkins NJ, Whitcomb BW, Schisterman EF. Youden Index and optimal cut-point estimated from observations affected by a lower limit of detection. Biom J 2008;50:419-30.
37. Zhou Y, Xu J, Liu Q, Li C, Liu Z, Wang M, Zheng H, Wang S. A Radiomics Approach With CNN for Shear-Wave Elastography Breast Tumor Classification. IEEE Trans Biomed Eng 2018;65:1935-42.
38. DeLong ER, DeLong DM, Clarke-Pearson DL. Comparing the areas under two or more correlated receiver operating characteristic curves: a nonparametric approach. Biometrics 1988;44:837-45.
39. Sun R, Hou X, Li X, Xie Y, Nie S. Transfer Learning Strategy Based on Unsupervised Learning and Ensemble Learning for Breast Cancer Molecular Subtype Prediction Using Dynamic Contrast-Enhanced MRI. J Magn Reson Imaging 2022;55:1518-34.
40. Chou SS, Gombos EC, Chikarmane SA, Giess CS, Jayender J. Computer-aided heterogeneity analysis in breast MR imaging assessment of ductal carcinoma in situ: Correlating histologic grade and receptor status. J Magn Reson Imaging 2017;46:1748-59.
41. Gerlinger M, Rowan AJ, Horswell S, Math M, Larkin J, Endesfelder D, et al. Intratumor heterogeneity and branched evolution revealed by multiregion sequencing. N Engl J Med 2012;366:883-92.
42. Mahrooghy M, Ashraf AB, Daye D, Mies C, Feldman M, Rosen M, Kontos D. Heterogeneity wavelet kinetics from DCE-MRI for classifying gene expression based breast cancer recurrence risk. Med Image Comput Comput Assist Interv 2013;16:295-302.
43. Li L, Wang K, Sun X, Wang K, Sun Y, Zhang G, Shen B. Parameters of dynamic contrast-enhanced MRI as imaging markers for angiogenesis and proliferation in human breast cancer. Med Sci Monit 2015;21:376-82.
44. Bedard PL, Hansen AR, Ratain MJ, Siu LL. Tumour heterogeneity in the clinic. Nature 2013;501:355-64.
45. Guo Y, Hu Y, Qiao M, Wang Y, Yu J, Li J, Chang C. Radiomics Analysis on Ultrasound for Prediction of Biologic Behavior in Breast Invasive Ductal Carcinoma.

 

Clin Breast Cancer 2018;18:e335-44.
46. Grossmann P, Stringfield O, El-Hachem N, Bui MM, Rios Velazquez E, Parmar C, Leijenaar RT, Haibe-Kains B, Lambin P, Gillies RJ, Aerts HJ. Defining the biological basis of radiomic phenotypes in lung cancer. Elife 2017;6:e23421.
47. Tran B, Dancey JE, Kamel-Reid S, McPherson JD, Bedard PL, Brown AM, Zhang T, Shaw P, Onetto N, Stein L, Hudson TJ, Neel BG, Siu LL. Cancer genomics: technology, discovery, and translation. J Clin Oncol 2012;30:647-60.
48. Kuo MD, Gollub J, Sirlin CB, Ooi C, Chen X. Radiogenomic analysis to identify imaging phenotypes associated with drug response gene expression programs in hepatocellular carcinoma. J Vasc Interv Radiol 2007;18:821-31.
49. Rutman AM, Kuo MD. Radiogenomics: creating a link between molecular diagnostics and diagnostic imaging. Eur J Radiol 2009;70:232-41.
50. Zardavas D, Irrthum A, Swanton C, Piccart M. Clinical management of breast cancer heterogeneity. Nat Rev Clin Oncol 2015;12:381-94.
51. Orlando L, Viale G, Bria E, Lutrino ES, Sperduti I, Carbognin L, Schiavone P, Quaranta A, Fedele P, Caliolo C, Calvani N, Criscuolo M, Cinieri S. Discordance in pathology report after central pathology review: Implications for breast cancer adjuvant treatment. Breast 2016;30:151-5.
52. Luo WQ, Huang QX, Huang XW, Hu HT, Zeng FQ, Wang W. Predicting Breast Cancer in Breast Imaging Reporting and Data System (BI-RADS) Ultrasound Category 4 or 5 Lesions: A Nomogram Combining Radiomics and BI-RADS. Sci Rep 2019;9:11921.
53. Yu Y, Tan Y, Xie C, Hu Q, Ouyang J, Chen Y, et al. Development and Validation of a Preoperative Magnetic Resonance Imaging Radiomics-Based Signature to Predict Axillary Lymph Node Metastasis and Disease-Free Survival in Patients With Early-Stage Breast Cancer. JAMA Netw Open 2020;3:e2028086.
54. Wang X, Xie T, Luo J, Zhou Z, Yu X, Guo X. Radiomics predicts the prognosis of patients with locally advanced breast cancer by reflecting the heterogeneity of tumor cells and the tumor microenvironment. Breast Cancer Res 2022;24:20.
55. Xie Y, Chen F, Li H, Wu Y, Fu H, Zhong Q, Chen J, Wang X. Development and validation of a clinical-radiomics nomogram for predicting a poor outcome and 30-day mortality after a spontaneous intracerebral hemorrhage. Quant Imaging Med Surg 2022;12:4900-13.
56. Li C, Yin J. Radiomics Nomogram Based on Radiomics Score from Multiregional Diffusion-Weighted MRI and Clinical Factors for Evaluating HER-2 2+ Status of Breast Cancer. Diagnostics (Basel) 2021.
57. Nie P, Yang G, Wang Z, Yan L, Miao W, Hao D, Wu J, Zhao Y, Gong A, Cui J, Jia Y, Niu H. A CT-based radiomics nomogram for differentiation of renal angiomyolipoma without visible fat from homogeneous clear cell renal cell carcinoma. Eur Radiol 2020;30:1274-84.
58. Tang TY, Li X, Zhang Q, Guo CX, Zhang XZ, Lao MY, Shen YN, Xiao WB, Ying SH, Sun K, Yu RS, Gao SL, Que RS, Chen W, Huang DB, Pang PP, Bai XL, Liang TB. Development of a Novel Multiparametric MRI Radiomic Nomogram for Preoperative Evaluation of Early Recurrence in Resectable Pancreatic Cancer. J Magn Reson Imaging 2020;52:231-45.
59. Zhou J, Luo LY, Dou Q, Chen H, Chen C, Li GJ, Jiang ZF, Heng PA. Weakly supervised 3D deep learning for breast cancer classification and localization of the lesions in MR images. J Magn Reson Imaging 2019;50:1144-51.

**Cite this article as:** Feng S, Yin J. Dynamic contrast-enhanced magnetic resonance imaging radiomics analysis based on intratumoral subregions for predicting luminal and nonluminal breast cancer. Quant Imaging Med Surg 2023;13(10):6735-6749. doi: 10.21037/qims-22-1073

 

## Appendix 1

### *Imaging protocol*

DCE-MRI was performed at 3.0 T using a Signa HDxt 3.0 T MRI scanner (GE HealthCare, Chicago, IL, USA). All patients were in prone position and were scanned with a dedicated 8-channel double breast coil. First, the axial fat saturation T1-weighted precontrast scanning based on VIBRANT-VX technology was obtained. After intravenous injection of a contrast agent (Magnevist, Bayer Healthcare Pharmaceuticals, Berlin, Germany) at 4 mL/s and a dose of 0.15 mmol/kg body weight, 8 postcontrast scans were obtained under the following parameters: repetition time, 7.42 ms; flip angle, 15°; echo time, 4.25 ms; slice thickness, 2.20 mm; spacing between slices, 2.20 mm; field of view, 340×340 $mm^2$; time per volume, 80s; and slice number, 78. Finally, 8 subtraction sequences were acquired by subtracting each precontrast scan sequence from the 8 postcontrast scan sequences.

### *Tumor segmentation*

Two radiologists with 5 years (reader 1) and 10 years (reader 2) of working experience in breast MRI diagnosis evaluated the subtraction sequences of the fourth stage blinded to the pathological results of the patients; the section with the largest tumor cross-sectional area was selected from the image data of each patient for subsequent analysis. In case of judgment discrepancy, a third physician with 15 years (reader 3) of diagnostic experience made a final decision. MATLAB 2018b (MathWorks, Natick, MA, USA) was used to semiautomatically segment the selected slices to obtain the whole tumor region. First, readers 1 and 2 delineated an arbitrarily shaped region of interest (ROI) around the lesion area on the slice. Then, the pixel gray value in the ROI was normalized to average gray value of the pixels in the region of interest with a standard deviation of 3, and the region was quantized to 8 bits per pixel to change the signal-to-noise ratio of the texture results. Finally, the spatial fuzzy C-means (FCM) algorithm was applied to depict the contour boundary of the lesion according to the ROI, and the details were improved via morphological processing of the whole lesion area. In addition, for tumors near the edge of the breast or chest wall, a breast parenchyma ROI was manually created using ITK-SNAP software (www.itksnap.org) and loaded into MATLAB 2018b.

### *Pathologic assessment*

ER, PR, and HER2 expression was detected with streptavidin peroxidase immunohistochemistry (IHC). The test results were interpreted by pathologists. ER or PR staining in at least 1% of tumor nuclei was defined as ER or PR positivity (60). HER2 expression results of a single negative or single positive were considered HER2 negative, triple positive was considered HER2 positive, and double positive was further verified with fluorescence *in situ* hybridization (61). According to ER and PR expression, cases were divided into luminal type (ER positive and/or PR positive) and nonluminal type (ER negative and PR negative).

### *Rad score calculation formula in predicting luminal and nonluminal breast cancer*

Rad-score = 0.6969 +
–0.5428 × S-8_Rapid_Skewness+
0.3935 × S-4_ Rapid _SRHGLE_0+
–0.3304 × S-4_ Rapid _GLN_135 +
–0.4182 × S-0_ Rapid_Skewness+
0.1870 × S-0_ Rapid _ Deubechies2_4_H_V

## References

60. Hammond ME, Hayes DF, Wolff AC, Mangu PB, Temin S. American society of clinical oncology/college of American

 https://dx.doi.org/10.21037/qims-22-1073

pathologists guideline recommendations for immunohistochemical testing of estrogen and progesterone receptors in breast cancer. J Oncol Pract 2010;6:195-7.
61. Wolff AC, Hammond MEH, Allison KH, Harvey BE, McShane LM, Dowsett M. HER2 Testing in Breast Cancer: American Society of Clinical Oncology/College of American Pathologists Clinical Practice Guideline Focused Update Summary. J Oncol Pract 2018;14:437-41.

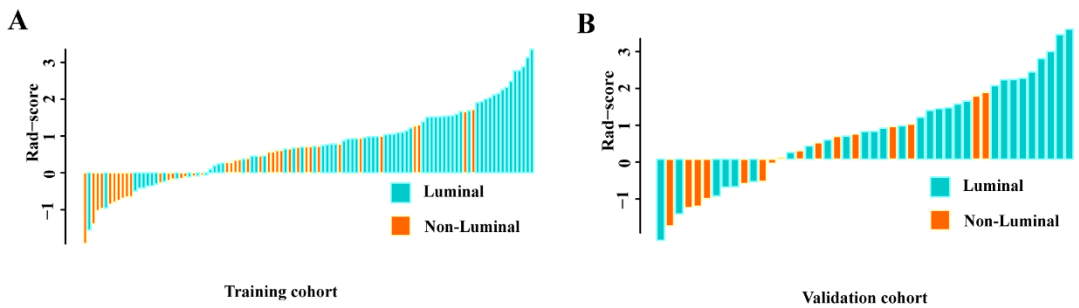


**Figure S1** Bar graph of the radiomics score of each patient in the training (A) and validation cohorts (B). For a detailed description of the features we extracted, please refer to the pyradiomics website (https://pyradiomics.readthedocs.io/en/latest/features.html).

**Table S1** Statistical comparison of AUC values between the 2 classifier models using the Delong test

| Model | Cohort | Regions | Rapid | Medium | Slow | Combined | Whole lesion |
|---|---|---|---|---|---|---|---|
| SVM | Training | Rapid | / | 0.126 | 0.629 | 0.120 | 0.322 |
| | | Medium | 0.126 | / | 0.667 | 0.016 | 0.635 |
| | | Slow | 0.629 | 0.667 | / | 0.177 | 0.177 |
| | | Combined | 0.120 | 0.016 | 0.177 | / | 0.081 |
| | | Whole lesion | 0.322 | 0.635 | 0.177 | 0.081 | / |
| | Validation | Rapid | / | 0.459 | 0.431 | 0.275 | 0.154 |
| | | Medium | 0.459 | / | 0.886 | 0.930 | 0.631 |
| | | Slow | 0.431 | 0.886 | / | 0.929 | 0.459 |
| | | Combined | 0.275 | 0.930 | 0.929 | / | 0.422 |
| | | Whole lesion | 0.154 | 0.631 | 0.459 | 0.421 | / |
| LR | Training | Rapid | / | 0.061 | 0.839 | 0.101 | 0.023 |
| | | Medium | 0.061 | / | 0.039 | 0.001 | 0.744 |
| | | Slow | 0.839 | 0.039 | / | 0.100 | 0.047 |
| | | Combined | 0.101 | 0.001 | 0.100 | / | 0.003 |
| | | Whole lesion | 0.023 | 0.744 | 0.047 | 0.003 | / |
| | Validation | Rapid | / | 0.261 | 0.288 | 0.254 | 0.254 |
| | | Medium | 0.261 | / | 0.759 | 0.675 | 0.962 |
| | | Slow | 0.288 | 0.759 | / | 0.725 | 0.735 |
| | | Combined | 0.254 | 0.675 | 0.725 | / | 0.647 |
| | | Whole lesion | 0.254 | 0.962 | 0.735 | 0.647 | / |

LR, logistic regression; SVM, support vector machine. The slash indicates that there is no data point here.


https://dx.doi.org/10.21037/qims-22-1073